

Geometrical spin manipulation in Dirac flakes

Ioannis Klefogiannis* and Ilias Amanatidis

Department of Electrophysics, National Chiao Tung University, Hsinchu 30010, Taiwan, Republic of China

We investigate numerically the spin properties of electrons in flakes made of materials described by the Dirac equation, at the presence of intrinsic spin-orbit-coupling(SOC). We show that electrons flowing along the borders of flakes via edge states, become helically spin-polarized for strong SOC, for materials with and without a gap at the Fermi energy, corresponding to the massive and massless Dirac equation respectively. The helically spin-polarized electrons cause geometrical spin splitting on opposite sides of the flakes, leading to spin-resolved transport controlled by the flake's geometry in a multi-terminal device setup. A simple analytical model containing the basic ingredients of the problem is introduced to get an insight of the helical mechanism, along with our numerical results which are based on an effective tight-binding model.

PACS numbers: 72.80.Vp, 71.70.Ej, 75.76.+j, 73.63.Kv

INTRODUCTION

Mesoscopic low-dimensional materials described by the Dirac equation for relativistic particles is a rapidly developing field providing a vast area of fundamental research and promising a wide range of applications. One of the earliest examples is graphene, a two-dimensional (2D) sheet of carbon atoms arranged in a honeycomb lattice structure resulting in an electronic behavior at the Fermi level that resembles relativistic massless particles described by the massless Dirac equation [1, 2]. Another more recent example is transition metal dichalcogenide (TMD) monolayers[3–11], with honeycomb lattice structure similar to graphene but with a varying gap at the Fermi level, for instance 1.35 eV for WS₂ and 1.83 eV for MoS₂. Alternatively a considerable gap of up to 0.278 eV can be created in graphene by embedding it on boron nitride (BN) substrates[12–14]. Graphene on BN substrates and TMD monolayers can be effectively described by the massive Dirac equation, instead of the massless one which describes pristine graphene.

Dirac materials can be easily formed in confined dot-like structures of various sizes and shapes, known as flakes, having been studied theoretically and demonstrated experimentally [1, 15–26]. Specifically for TMD flakes the trigonal shape is a natural state in their experimental preparation[25, 26]. The confinement in Dirac flakes leads to unconventional electronic properties such as the edge states, whose electronic density is concentrated at the edges of the flakes [16–18, 27] leading to novel topological phenomena [28–31]. Edge states are fundamentally a consequence of the honeycomb lattice morphology present in Dirac materials that favors destructive interference effects when zig-zag edges are present.

On the other hand spin-orbit-coupling(SOC) in Dirac materials offers the possibility to manipulate the electron spin for integration in spintronic applications [32–35]. Despite the weak SOC in graphene, the interaction with the system's confinement, particularly in graphene

nanoribbons, has been shown to produce novel quantum phases like the Quantum-Spin-Hall(QSH) effect[36–38]. The QSH effect has sparked a continuously increasing interest in exotic materials that display related behaviors known as topological insulators. Also spin-transport effects have been investigated in graphene flakes via DFT simulation[39, 40]. In the same sense, TMD monolayers and other emergent 2D materials are also promising candidates for relevant theoretical investigations[41] and applications since the SOC strength can be much higher than graphene, leading to large spin-splittings up to 0.46 eV in some cases of TMD monolayers[42].

In the current work we analyze the spin properties of electrons in Dirac flakes with intrinsic SOC via the numerical calculation of the transmission probabilities along the border of the flakes. We show that for sufficiently strong SOC the electrons that propagate in opposite directions along the flake's border via the edge states, have opposite spins, leading to helically spin-polarized electrons. We demonstrate this property in a multi-terminal device setup naturally formed by attaching three leads at the corners of a trigonal flake. Appropriate tuning of the chemical potential of the leads creates spin-resolved electronic transport with opposite spin-polarization along the opposite sides of the triangle. This allows a geometrical manipulation of the spin intrinsically without the need to apply external fields. The helically spin-polarized electrons are present in materials with and without a gap at the Fermi energy, described by the massive and massless Dirac equation, respectively, which could correspond to TMD monolayers and graphene. Additionally, we introduce a simplified analytical model, that contains the fundamental ingredients of the numerical model, allowing us to get a better understanding of our numerical results.

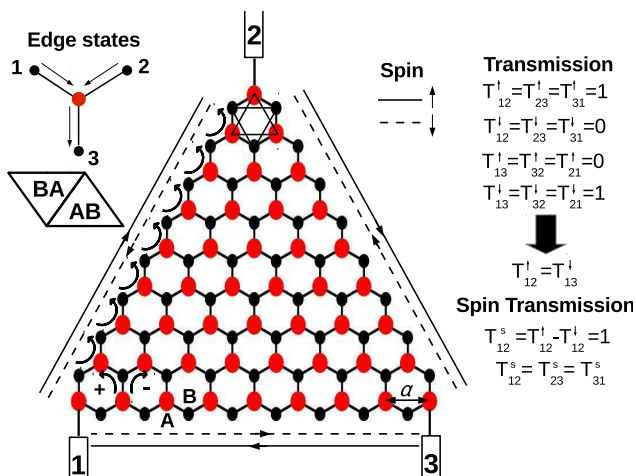


FIG. 1. A trigonal Dirac flake with the characteristic honeycomb lattice structure consisting of two sublattices A and B. An example of the spin-orbit coupling interaction involving spin-dependent hopping amplitude between second-nearest neighbor sites can be seen inside a single hexagon. Three leads can be attached naturally to the corners of the trigonal flake. The arrows across the flake's border indicate the helically spin-polarized electronic flow, satisfying the relations for the transmission probabilities between different terminals, shown on the right. We characterize the flake size by the length L of the triangle base, in units of the lattice constant a . The edge state mechanism due to the honeycomb lattice structure can be seen on the left along with a schematic showing how to exchange the A and B atoms by cutting the flake in different orientations.

MODEL

In this section, we present our numerical tight-binding model to simulate flakes made out of Dirac materials at the presence of SOC. Dirac materials can be described by the massive Dirac Hamiltonian[41, 43–47]

$$\mathcal{H}_0 = \hbar v_f (k_x \tau_z \sigma_1 + k_y \sigma_2) + V \sigma_3 \quad (1)$$

where v_f is the Fermi velocity of electrons whose value depends on the material under investigation, and σ_i being the Pauli matrices acting on orbital space. Symbol $\tau_z = \pm 1$ denotes the non-equivalent valleys that are present in graphene and other Dirac materials like TMD monolayers, at the six corners of their hexagonal Brillouin zone. Eq. 1 describes relativistic particles of mass V , while the speed of light c is replaced by v_f . Different values of V classify different materials for example $V = 0$ meV and $v_f \approx 10^6$ m/s corresponds to graphene, while finite V could describe TMD monolayers and graphene on BN substrates[14, 41, 43, 44].

In order to perform our numerical calculations, we consider an effective tight-binding model, consisting of a honeycomb lattice with first nearest neighbor hopping, along with an onsite staggered potential simulating the mass

term in Eq. 1,

$$H_0 = \sum_i \epsilon_i c_{i\mu}^\dagger c_{i\mu} + \sum_{\langle i,j \rangle} t_{i,j} (c_{i\mu}^\dagger c_{j\mu} + c_{j\mu}^\dagger c_{i\mu}), \quad (2)$$

where $c_{i\mu}^\dagger$ ($c_{i\mu}$) is the creation (annihilation) operator for spin μ at site i while $t_{i,j} = 1$ eV is a uniform hopping between all the nearest neighbor lattice sites. The onsite potential ϵ_i is V and $-V$ on A and B sublattice sites respectively with $V = 0$ corresponding to graphene. The staggered potential breaks the inversion symmetry resulting in a gap $2V$ at the Fermi energy for infinite unbounded systems. At low energies the effective tight-binding Hamiltonian Eq. 2 transforms to Eq. 1 with $\hbar v_f = \frac{t\sqrt{3}a}{2}$ where a is the lattice constant. This effective tight-binding model can be thought as a numerical version of the massive Dirac equation.

The SOC can be introduced in the tight-binding model by considering spin-dependent hoppings along next nearest neighbors in the honeycomb lattice as[36, 43],

$$H_{SOC} = \alpha \sum_{\langle\langle i,j \rangle\rangle, \mu, \mu'} \nu_{i,j} c_{i\mu}^\dagger s_{z, \mu, \mu'} c_{j\mu'}, \quad (3)$$

where the sum runs over next nearest neighbors on all the lattice sites. The spin-dependent amplitude is $\nu_{i,j} = 1(-1)$ when the electron at site i makes a anti-clockwise(clockwise) turn in order to hop from the first nearest to the second nearest neighbor j , represented by the curved arrows inside the honeycomb lattice of the trigonal flake in Fig. 1. The strength of the intrinsic SOC is determined by α . We note that the SOC interaction described by Eq. 3 involves connections between sites belonging to the same sublattices A or B, in conjunction with the first nearest neighbor term in Eq. 2 which involves connections only between A and B sublattice sites. Eq. 3 is responsible for the QSH effect in confined graphene systems, acting as a bridge between graphene and topological insulators. The total Hamiltonian of our system is

$$H = H_0 + H_{SOC}. \quad (4)$$

By applying hard-wall boundary conditions on Eq. 4 we can simulate the trigonal flakes, like the one shown in Fig. 1.

In order to calculate the transmission probabilities via the edges of the trigonal flake, we attach perfect semi-infinite linear chains described by $H_{1d} = \sum t(c_{i\mu}^\dagger c_{i+1\mu} + c_{i+1\mu}^\dagger c_{i\mu})$, with hopping $t=1$ eV at its three corners as shown in Fig. 1, forming this way a three terminal device. The energy E , the SOC strength α and V , are all reported in units of t . We observe that Eq. 3 contains only s_z so that the total Hamiltonian of the system Eq. 4 can be split in spin up and down diagonal blocks, resulting in zero transmission probability between opposite

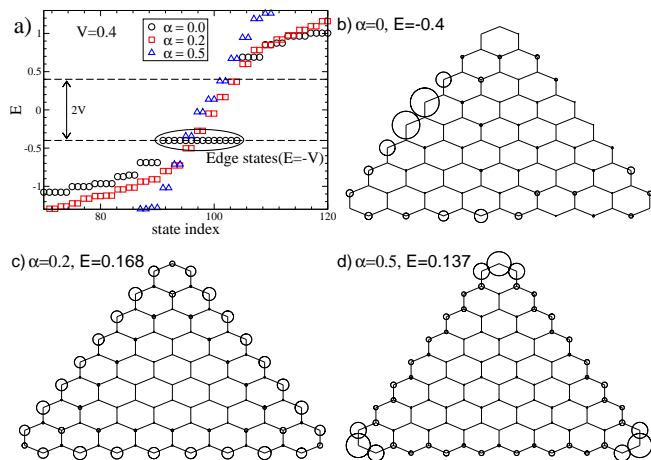


FIG. 2. a) The energy levels of a triangular Dirac flake for $L=8$, $V=0.4$ and different SOC strengths α near the gap induced by V . Fourteen edge states at $E=-V$ can be distinguished for $\alpha = 0$ due to sublattice symmetry, dispersing inside the gap for finite α . The levels become almost homogeneously distributed for large α . b) The respective wavefunction for $\alpha = 0$ at $E=-V$ is an edge state being non-zero only on B sublattice sites. c) The edge state is enhanced by the SOC becoming completely concentrated at the edges. d) The wavefunction is accumulated at the corners for large α .

spins(see Appendix). Therefore the transmission probability between different terminals can be written as T_{ij}^μ where $i,j=1,2,3$ runs over the terminals and $\mu = \uparrow, \downarrow$ denotes the spin orientation of the electron. We define also the spin transmission as $T_{ij}^s = T_{ij}^\uparrow - T_{ij}^\downarrow$ which can be used to estimate the degree of spin-polarization. T_{ij}^μ can be calculated by using the Green's function $\mathcal{G}(i, j, \mu, E) = (E^+ - H - \Sigma_1(E^+) - \Sigma_2(E^+) - \Sigma_3(E^+))^{-1}$ with $E^+ = E + i\eta$, where E is the incident energy and $\eta \rightarrow 0^+$, while $\Sigma_i(E)$ is the self energy of each semi-infinite chain used as leads, being diagonal in the spin-basis, since we neglect the SOC inside the leads(see Appendix). By using the velocities inside the leads according to the Fisher-Lee relations we get $T_{ij}^\mu = (4 - E^2)|\mathcal{G}(j, i, \mu, E)|^2$.

EDGE STATES

In this section, we analyze the edge states present in the trigonal zig-zag flakes made of Dirac materials, which are responsible for the electronic behavior near the Fermi level. In the lattice representation, the number of edge states can be derived by extending chiral symmetry arguments applied on the honeycomb lattice which is bipartite[48]. In general the Dirac flakes can be split into two sublattices with N_A number of A and N_B number of B sublattice sites, as shown in Fig. 1. The type of the outermost atoms at the zig-zag edges of the flake determines which number, either N_A or N_B is larger. For

the configuration in Fig. 1 with B type atoms, we have $N_B > N_A$, while $N_B - N_A = L - 1$, with L being the length of the triangle basis in units of the lattice constant a . We note that the type of atoms A and B can be easily exchanged by changing the orientation of the triangle base on an infinite graphene sheet by 60 degrees, compared to the base of the flake in Fig. 1, resulting in $N_A > N_B$ in this case. Since the spin-orbit coupling given by Eq. 3 contains only s_z it does not mix the spin up with the spin down orientations, so that the total Hamiltonian of the system can always be split into spin up and spin down diagonal blocks. Consequently we can write down the Schrödinger difference equations centered on A and B atoms for spin up(down) denoted by $\mu = 1(-1)$ as,

$$\begin{aligned} (E - \epsilon_A)\Psi_{A,i}^\mu &= t \sum_j \Psi_{B,j}^\mu + i\mu\alpha \sum_j \nu_{i,j} \Psi_{A,j}^\mu \\ (E - \epsilon_B)\Psi_{B,i}^\mu &= t \sum_j \Psi_{A,j}^\mu + i\mu\alpha \sum_j \nu_{i,j} \Psi_{B,j}^\mu \end{aligned} \quad (5)$$

where $\Psi_{A(B),i}$ is the wavefunction amplitude on site i of each sublattice and $\epsilon_{A(B)}$ is the staggered on-site potential. In both sets of equations, the first term on the right-hand side comes from the nearest neighbour hopping, while the second term is associated with the second nearest neighbor hopping with spin dependent amplitude $\nu_{i,j}$, as in Eq. 3. In the absence of SOC ($\alpha = 0$), we can easily derive the number of edge states by algebraic arguments applied on Eq. 5. For $\epsilon_A = V, \epsilon_B = -V$ the equations become,

$$(E - V)\Psi_{A,i}^\mu = t \sum_j \Psi_{B,j}^\mu \quad (6.1)$$

$$(E + V)\Psi_{B,i}^\mu = t \sum_j \Psi_{A,j}^\mu. \quad (6.2)$$

Eq. 6.1 is a set of N_A equations with N_B unknowns written on the A sites, while Eq. 6.2 is a set of N_B equations with N_A unknowns written on the B sites, respectively. We observe that for $E=-V$, Eq. 6.2 transforms to the homogeneous set $0 = t \sum_k \Psi_{A,k}^\mu$ which can only be satisfied by assuming that $\Psi_A^\mu = 0$ since there are more equations than unknowns. On the other hand Eq. 6.1 transforms to $-2V\Psi_A^\mu = t \sum_k \Psi_{B,k}^\mu \Rightarrow 0 = t \sum_k \Psi_{B,k}^\mu$ which gives Ψ_B^μ , but results also in $N_B - N_A$ linearly independent solutions, since there are less equations than unknowns.

Consequently for $\alpha = 0$ there are at least $N_B - N_A$ states at $E=-V$ with non-zero amplitudes only on the B sublattice sites. For $V=0$ we derive the well-known case of bipartite lattices where there are at least $N_B - N_A$ states at $E=0$ due to the chiral symmetry[48]. With the application of the staggered potential ($V \neq 0$) the energy of these states is shifted to $E=-V$. Considering the spin these states become doubly degenerate.

Due to the destructive interference effects favored by the honeycomb lattice when zig-zag edges are present, these states either at $E=-V$ or $E=0$ are edge states with their corresponding wavefunctions concentrated at zig-zag edges of the flakes. The edge state mechanism can be robustly understood by isolating part of the zig-zag edge as shown in Fig. 1 at the right side of the flake schematic, where there are three B sites surrounding one A site. The edge states can be visualized as two incoming electronic waves from two B sites 1 and 2, interfering and giving an outgoing wave at site 3 via the A site. For $E=0$ there is destructive interference of the two incoming waves due to a phase difference between the wavefunction amplitudes on the respective sites 1 and 2, introduced by the Bloch's theorem, as can be seen easily in a semi-infinite graphene sheet with one zig-zag edge[27]. These two waves from sites 1 and 2 interfere destructively via the central A site whose wavefunction is zero, giving zero amplitude at site 3 for states at the ends of the Brillouin zone where the phase difference is π or a reduced amplitude otherwise. This interference process continues inside the rest of the honeycomb lattice and is present whenever zig-zag edges exist at the borders of a confined graphene structure. The application of the staggered potential, does not alter this basic topology of the honeycomb lattice structure which is responsible for the edge states, since it gives a potential $-V$ on all the B sites 1,2,3 and potential V on site A, resulting in the shifting of the edge state mechanism to energy $E=-V$. We note that the interference mechanism responsible for the edge states vanishes for the armchair edge morphology.

According to the above algebraic arguments, the energy of the edge states can be shifted at the opposite (conduction) side of the energy spectrum at $E=V$ by simply exchanging the potential on A and B sublattice sites, so that the outermost sites at the zig-zag edges in Fig. 1 have on-site potential V instead of $-V$. We summarize that for Dirac flakes with zig-zag edges, in the absence of SOC, there are at least $|N_A - N_B|$ edge states at $E=V(E=-V)$ when the potential of the outermost atoms of the zig-zag edges is $V(-V)$. Therefore, there are always edge states whose energy is determined by the type of atoms at the zig-zag edges of the flake, while their number increases linearly with the system size L as $|N_A - N_B| = L - 1$. In realistic systems, our results imply that the energy of the edge states can be tuned near either the valence or the conduction band edge, by appropriately cutting the Dirac flakes, in such a way that the type of atoms A and B are exchanged.

When the SOC is introduced in the system, for $\alpha \neq 0$ in Eq. 5, the edge states disperse inside the gap created either, due the staggered potential V , or due to the finite flake size. For instance, this phenomenon has been observed in MoS_2 flakes by multi-orbital tight-binding simulation[24]. In our case this behavior can be understood by the SOC term in Eq. 5 which alters the values

of E for which these equations can be satisfied according to the algebraic arguments we presented. The energy $E=-V$ is no longer a solution of these equations, while the wavefunction amplitude becomes gradually finite on both sublattice sites A and B as α is increased. In the simulation of specific materials the SOC term Eq. 3 has to be applied only on one of the sublattices. If it is applied only on A then the results we derived for $\alpha = 0$ remain valid, since the wavefunction amplitude on A sites is zero and any perturbation applied on this sublattice will not affect the system's properties.

We have verified our analytical results numerically. An example can be seen in Fig. 2a where the energy levels for a trigonal flake with $L=8$ and $V=0.4$ are shown, near the energy gap. All states come in pairs due to the spin degeneracy, which is preserved even for finite α . In agreement with our algebraic arguments there are $2(N_B - N_A) = 14$ edge states at $E=-V$, which disperse inside the gap for finite α . For sufficiently large α the states tend to repulse, becoming almost homogeneously distributed inside the whole gap, despite being initially concentrated at its lower end($E=-V$). In general a significant interplay between the SOC and the gap generated by the staggered potential is expected. Additionally the edge states due to zig-zag edges become gradually mixed with the edge states created due to the SOC in analogy to the edge state mechanism in the Quantum-Hall effect. In this sense, the edge state mechanism originating from the honeycomb lattice structure is enhanced by the SOC, however its contribution becomes irrelevant for strong SOC.

Some examples of these edge states can be seen in Fig. 2b,c,d where the wavefunction probability is shown, represented by the radius of circles at each site. For $\alpha = 0$ the amplitude of the edge state at $E=-0.4$, is non-zero only on the B sites, with the largest amplitude residing along the edges. There is almost perfect concentration of the wavefunction at the zig-zag edges of the flakes for finite α . A gradual accumulation at the corners of the triangle can be observed for large SOC ($\alpha = 0.5$). This is due to the different lattice connectivity between the sites at the corners of the triangle and the ones along the zig-zag edge. Particularly the corner sites are connected via two spin-dependent hoppings to second nearest neighbors, instead of four for sites along the zig-zag edge, coming from Eq. 3. Also, each of the corners can be thought as the intersection between two zig-zag chains causing additional interference effects, that cannot be distinguished for $\alpha = 0$ since the wavefunction probability is zero on A sites. We note that the results are similar for the spin up and down cases.

TRANSMISSION PROBABILITIES

In the current section we investigate the transmission probabilities via the edges of the trigonal Dirac flakes

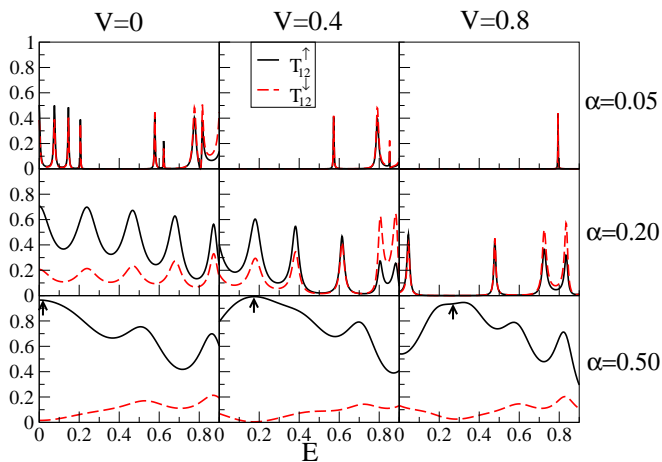


FIG. 3. The transmission probabilities T_{12}^{μ} between terminals 1 and 2 for spin up and down, different α and V . For strong SOC $\alpha = 0.5$ a significant difference between up and down is formed indicated by an arrow where $T_{12}^{\uparrow} \approx 1$ and $T_{12}^{\downarrow} \approx 0$, signifying helically fully spin-polarized electrons flowing along the edge. The helical regime is shifted along the energy for increasing V .

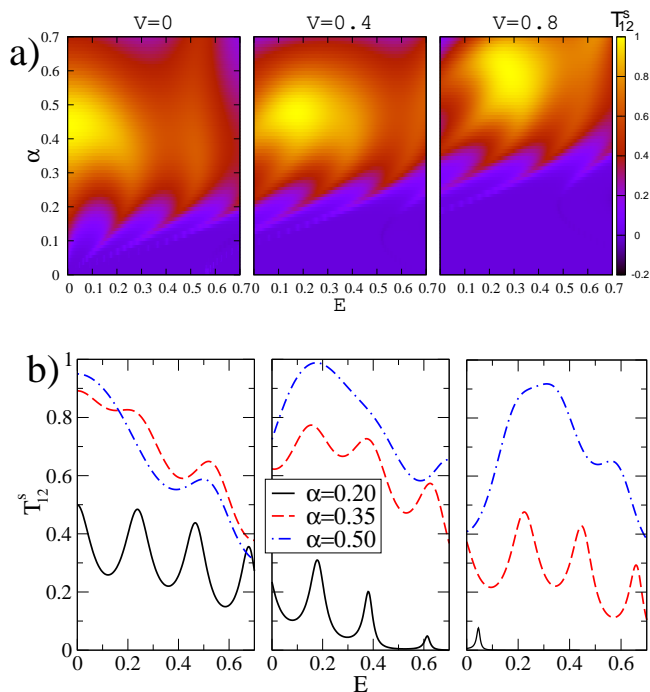


FIG. 4. a) Density color plot of the spin transmission versus E and α . Inside the yellow area where $T_{12}^s \approx 1$ the electrons are helically spin polarized. Larger α is required for materials with wider gaps (larger V) in order to observe the helicity. b) Some respective cases of T_{12}^s versus E for different α .

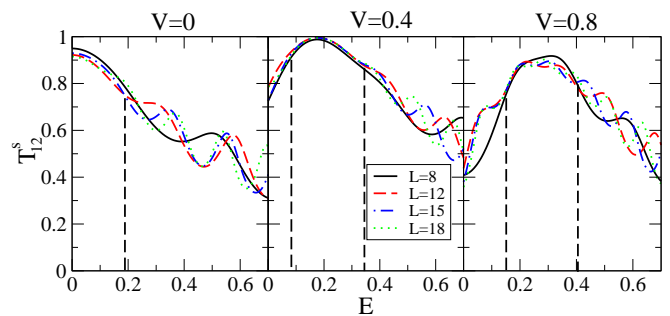


FIG. 5. T_{12}^s for $\alpha = 0.5$ and different flake sizes L . The helical regime is retained for all L independently of V .

with SOC. In order to probe the transmission we form a three terminal device setup by attaching linear chains at the three corners of the triangle, as shown in Fig. 1. In Fig. 3 we show the spin-dependent transmission probabilities T_{12}^{μ} for $L=8$ along one side of the triangle for terminal 1 to 2 for the spin-up and spin-down cases. We have performed the calculation for different values of the staggered potential V and the SOC strength α . The electronic flow inside the energy area where we plot our results, is carried via edge states like the ones in Fig. 2 for finite α . For weak SOC ($\alpha = 0.05$) resonant transmission via the respective energy levels of the system can be seen as sharp peaks. Increasing α causes broadening of these peaks resulting in the smooth fluctuations shown. Clearly, a significant difference between the opposite spins is starting to show for sufficiently large α . For $\alpha = 0.5$ a small regime is formed for every V , indicated with a small arrow, where there is almost perfect propagation of solely spin-up electrons ($T_{12}^{\uparrow} \approx 1, T_{12}^{\downarrow} \approx 0$). We note that large SOC interactions have been demonstrated in TMD monolayers[42] which correspond to finite V in our model.

This behavior can be attributed to two mechanisms. One is the helical currents at the edges induced by the QSH effect followed by the Laughlin's argument, in analogy with the zig-zag nanoribbons with SOC[36]. An additional mechanism can be revealed by a careful observation of the zig-zag edge. In Fig. 1 we can see that the electronic flow from terminal 1 to 2 is carried through the outermost B (black) sites via anticlockwise turns corresponding to positive spin-flip amplitude $\nu = +1$ in Eq. 3, implying spin-up polarization. The other possible flow via A (red) sites across the edge corresponding to spin-down polarization is partially suppressed since the wavefunction amplitude is generally smaller than on B sites, being a remnant of the chiral symmetry for $\alpha = 0$, as we have shown in the previous section.

The spin-polarized regime is shifted slightly by increasing V , due to the scattering via the positive potential V encountered by the incident electrons from the leads attached to the corners of the triangle. Potential V can be

thought as a barrier that the electrons need to overcome, by acquiring sufficiently large incident energy E . We have verified that the transmission probabilities T_{ij}^μ between different terminals satisfy the conditions $T_{ij}^\uparrow = T_{ji}^\downarrow$, which are a consequence of the triangle's symmetry. Combined with $T_{12}^\uparrow \approx 1, T_{12}^\downarrow \approx 0$ they lead to the conditions shown at the right side of Fig. 1. As long as these conditions are satisfied the electrons propagating in opposite directions along the edges of the flake, will have also opposite spins. In this sense, the electrons in the trigonal Dirac flakes become helically spin-polarized along the edge for sufficiently strong SOC. Additionally, we observe that the transmission is enhanced by the SOC due to the accumulation of the wavefunction at the corners of the triangle where the leads are attached, as can be seen in Fig. 2d. However the helicity suppresses the electronic flow for one of the spin orientations and consequently the total (charge) transmission remains almost one for every α at energies where the transmission occurs via the energy levels of the flake.

To further analyze the helical regime, in Fig. 4 we show a density color-plot of the spin transmission T_{12}^s versus E and α , along with individual cases for constant α in the bottom. The helical (yellow) regime can be clearly distinguished where T_{12}^s becomes maximum ($T_{12}^s = 1$), signifying fully spin-polarized electrons that propagate helically along the flake's edge. We notice that for larger V , corresponding to materials with wider gaps, larger SOC is needed in order to observe the helically polarized electrons. This is due to the interplay between the gap generated by the staggered potential and the one due to the SOC[36]. In order for the QSH effect to manifest, being essentially responsible for the helicity, the SOC has to dominate the gap over the staggered potential. The helical regime is retained for all flake sizes, ranging from tenth to a few hundred atoms, as can be seen in Fig. 5, with more fluctuations created, due to the denser energy levels as the size is increased.

By appropriately tuning the chemical potentials μ_i corresponding to each terminal i in the three-terminal setup[49], spin-polarized currents with opposite polarization flow along the opposite sides of the triangle. For $\mu_1 = \mu_3$ spin currents $I_1^s = -I_3^s = \frac{e}{4\pi}(\mu_1 - \mu_2)$ flow at terminals 1 and 3 with opposite spin polarizations. Therefore, spin-resolved transport along the different sides of the flake is possible, allowing in this sense a geometrical manipulation of the electron spin, since the path of the spin-polarized electrons can be controlled by the flake's shape.

We expect similar phenomena for differently shaped flakes such as hexagonal, which could offer additional possibilities to control the spin dependent transmission by attaching more leads at the flake's corners. Also impurities or weak disorder should not affect our results since the system is protected from backscattering due to

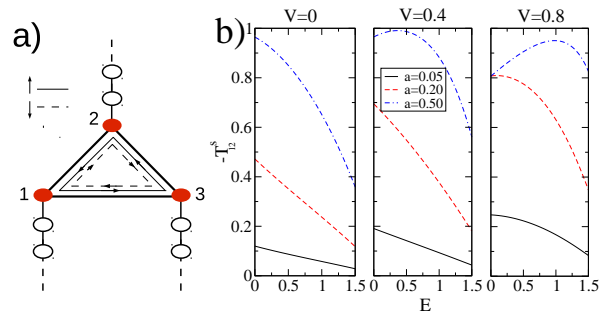


FIG. 6. a) A simple model simulating the three-terminal setup of the trigonal Dirac flake, the edge state mechanism along with the influence of the intrinsic SOC. b) T_{12}^s for different α and V . The curves describe the trend of the numerical results for all cases.

the time reversal symmetry, as in QSH systems.

In order to further investigate the helical mechanism we introduce a simple model consisting of a triangle with three sites with constant on-site potential V in analogy with the potential at the corners of the flake in Fig. 1 and three linear chains attached to its corners acting as leads, as shown in Fig. 6a. Also, we consider spin dependent hoppings of strength α inside the triangle simulating the SOC. This model can be considered as an isolation of the SOC mechanism for each of the sublattices A or B (Eq. 3) inside one hexagon in the honeycomb lattice, corresponding to $L=1$ for the trigonal Dirac flake. Alternatively it can be thought as a robust simulation of the numerical model, since it contains the basic ingredients of the problem, namely the fact that the electrons propagate in a straight orbit along the border of the trigonal flake due to the edge states, under the influence of the intrinsic SOC. We note that due to the way we oriented the triangle the transmission from site 1 to 2 T_{12}^s takes negative values. In Fig. 6b we show the spin transmission T_{12}^s for different V and SOC strengths. We show $-T_{12}^s$ in order to lie in the positive axis. The calculation details are presented in the Appendix. The analytical curves catch the trend of the numerical results for the trigonal flake with maximum $T_{12}^s \approx 1$ for sufficiently large α , which is shifted across the energy for finite V .

CONCLUDING REMARKS

We have presented a numerical study of the spin properties of electrons in flakes made of Dirac materials at the presence of intrinsic spin-orbit-coupling (SOC). A detailed analysis of the edge states is also presented, based on sublattice symmetry arguments. The flakes are simulated by an effective tight-binding model, which can be thought as a numerical version of the Dirac equation. We probe the spin dependent transport by forming a multi-

terminal device which allows the calculation of the transmission probabilities along the edges of the flakes via the Green's function formalism.

We have shown that the electrons propagating along the border of the flakes via the edge states, become helically spin polarized for strong SOC, for both the massless and massive cases, corresponding to Dirac materials with and without a gap at the Fermi energy, respectively. The helicity can be easily detected in a three-terminal setup formed naturally by attaching 1d leads at the corners of a trigonal flake. Appropriate tuning of the chemical potential of each lead, creates spin-resolved transport with opposite polarization between the opposite sides of the flakes, allowing a geometrical manipulation of the electron spin.

In other words, we have shown that spin-resolved transport can be created intrinsically in flakes made of Dirac materials by forming multi-terminal devices without the need of external fields, the only requirement being sufficiently strong intrinsic SOC. We hope that our work will motivate further investigation of the SOC effects in 2d materials in conjunction with topological effects due to confinement in flakes and other nano-structures.

ACKNOWLEDGEMENTS

We are grateful to Chi-Shung Tang, Shun-Jen Cheng and Victor A. Gopar for valuable discussions and careful reading of the manuscript. This work was supported by Ministry of Science and Technology, Taiwan through No. MOST 103-2112-M-239-001-MY3, MOST-103-2112-M-009-014-MY3, and National Science Council through No. NSC 102-2112-M-009-009-MY2. Also, we thank the Ministry of Education through the Aiming for Top University Plan (MOE ATU), and the National Center for Theoretical Sciences.

Appendix: Simple model

In the following Appendix, we present the derivation of the transmission probabilities for a simple system consisting of a triangle with three sites, and three linear chains attached to its corners acting as leads. We consider SOC inside the triangle by assuming spin-flip hopping of strength α between each site, denoting also the SOC strength in analogy with the numerical model. Spin-up(down) corresponds to $\mu = 1(-1)$.

The Hamiltonian of the system can be split in spin-up and spin-down blocks since the SOC does not mix the

two spins, as

$$H = \begin{pmatrix} h^\uparrow & 0 \\ 0 & h^\downarrow \end{pmatrix} \quad (7)$$

where h^\uparrow and h^\downarrow are,

$$h^\mu = \begin{pmatrix} V & 1 - i\mu\alpha & 1 + i\mu\alpha \\ 1 + i\mu\alpha & V & 1 - i\mu\alpha \\ 1 - i\mu\alpha & 1 + i\mu\alpha & V \end{pmatrix}, \quad (8)$$

by assuming real hopping $t=1$ eV between the three sites, with $\mu = 1(-1)$ for spin up(down). The transmission probabilities between the different sites of the triangle can be calculated via the Green's function

$$G(E) = (EI - H - \Sigma(E))^{-1} \quad (9)$$

where $\Sigma(E) = \Sigma_1(E) + \Sigma_2(E) + \Sigma_3(E)$ is the self-energy due to the semi-infinite linear chains at the corners described by $H = \sum_i c_i c_{i+1}^\dagger + c.c$ with energy dispersion $E = 2t\cos(k)$. $\Sigma(E)$ is given by equal diagonal blocks for spin up and down

$$\Sigma^\mu(E) = \begin{pmatrix} \Sigma_{1d}(E) & 0 & 0 \\ 0 & \Sigma_{1d}(E) & 0 \\ 0 & 0 & \Sigma_{1d}(E) \end{pmatrix} \quad (10)$$

where $\Sigma_{1d}(E)$ is the self-energy of each chain, which can be calculated recursively as follows [50].

In general we can calculate the Green's function via

$$G(E) = (E - g(E))^{-1}. \quad (11)$$

where $g(E)$ represents the surface Green's function of the semi-infinite chain. Adding a single site via hopping $t=1$ to the chain should not alter its Green's function, so that $G(E) = g(E)$. Consequently we can write the following recursive relation for $g(E)$,

$$g(E) = (E - g(E))^{-1} \Rightarrow g(E) = \frac{E}{2} \pm i\sqrt{1 - \frac{E^2}{4}}. \quad (12)$$

Since we are interesting only in the retarded Green's function we choose the minus sign representing outgoing waves from the point of excitation, giving the self-energy $\Sigma_{1d}(E) = g(E)$,

$$\Sigma_{1d}(E) = \frac{E}{2} - i\sqrt{1 - \frac{E^2}{4}} \text{ for } -2 < E < 2. \quad (13)$$

Since H and $\Sigma(E)$ are both block-diagonal in the spin basis, this is also true for Eq. 9. Therefore the Green's function elements between opposite spins are zero, and we can write

$$G^\mu(E) = (EI - h^\mu - \Sigma^\mu(E))^{-1} \quad (14)$$

By plugging Eq. 8, Eq. 10 in Eq. 14 and inverting, we derive the following formula for the Green's function element from site 1(excitation) to 2(response)

$$G_{21}^{\mu}(E) = -\frac{1 - \alpha^2 + E - \Sigma_{1d}(E) + i\mu\alpha(-2 + E - \Sigma_{1d}(E) - V) - V}{(2 - E + \Sigma_{1d}(E) + V)(-3\alpha^2 + (-1 - E + \Sigma_{1d}(E) + V)^2)}$$

In order to calculate the respective transmission probabilities we apply the Fischer-Lee relations,

$$T_{12}^{\mu}(E) = v(E)^2 |G_{21}^{\mu}(E)|^2 \quad (15)$$

where $v(E) = \frac{\partial E}{\partial k} = -2\sqrt{1 - \frac{E^2}{4}}$ is the group velocity of the linear chains, assuming that $\hbar = 1$. We note that the transmission probabilities between opposite spins are zero since the respective Green's function elements are zero.

By using the above relation we can calculate the spin transmission $T_{12}^s(E)$ which is plotted in Fig. 6

$$T_{12}^s(E) = \left(T_{12}^{\uparrow}(E) - T_{12}^{\downarrow}(E) \right). \quad (16)$$

REFERENCES

-
- * ioannis@ntu.edu.tw; Current address: Department of Physics and Center for Theoretical Sciences, National Taiwan University, Taipei 106, Taiwan
- [1] K. S. Novoselov, A. K. Geim, S. V. Morozov, D. Jiang, Y. Zhang, S. V. Dubonos, I. V. Grigorieva, A. A. Firsov, *Science* **306**, 666, (2004).
- [2] A. Castro Neto, F. Guinea, N. Peres, K. Novoselov, and A. Geim, *Rev. Mod. Phys.* **81**, 109 (2009).
- [3] R. F. Frindt, *J. Appl. Phys.* **37**, 1928 (1966).
- [4] A. Splendiani, L. Sun, Y. Zhang, T. Li, J. Kim, C. Chim, G. Galli and F. Wang, *Nano Lett.*, 2010, **1271** (2010).
- [5] B. Radisavljevic, A. Radenovic, J. Brivio, V. Giacometti, and A. Kis, *Nat. Nanotechnol.* **6**, 147 (2011).
- [6] N. Zibouche, A. Kuc and T. Heine, *Eur. Phys. J. B*, **85** 149 (2012).
- [7] C. Ataca, H. ahin, and S. Ciraci, *J. Phys. Chem. C*, **116**, 8983 (2012).
- [8] A. Castellanos-Gomez, M. Barkelid, A. M. Goossens, V. E. Calado, H. S. J. van der Zant, and G. A. Steele, *Nano Lett.* **12**, 3192 (2012).
- [9] K. Taniguchi¹, A. Matsumoto, H. Shimotani³ and H. Takagi, *Appl. Phys. Lett.* **101**, 109902 (2012).
- [10] Y. Huang *et al.*, *Nano Research* **6**, 200 (2013).
- [11] Yi-Hsien Lee *et al.*, *Nano Lett.*, 2013, 13, (2013).
- [12] Menno Bokdam, Taher Amlaki, Geert Brocks, and Paul J. Kelly, *Phys. Rev. B* **89**, 201404 (2014).
- [13] Pilkyung Moon and Mikito Koshino, *Phys. Rev. B* **90**, 155406 (2014).
- [14] L. A. Chizhova, F. Libisch, and J. Burgdrfer, *Phys. Rev. B* **90**, 165404 (2014).
- [15] T. Yamamoto, T. Noguchi, K. Watanabe, *Phys. Rev. B* **74** (12), 121409 (2006).
- [16] M. Ezawa, *Phys. Rev. B* **76**, 245415 (1-6) (2007)
- [17] W. L. Wang, S. Meng, and E. Kaxiras, *Nano Lett.* **8**, 241 (2008)
- [18] H. P. Heiskanen and M. Manninen, J. Akola, *New J. Phys.* **10**, 103015 (2008).
- [19] Akola J, Heiskanen H P and Manninen M., *Phys. Rev. B* **77**, 193410 (2008).
- [20] L. A. Ponomarenko *et al.*, *Science* **320**, 356 (2008).
- [21] J. Wu, W. Pisula, K. Müllen, *Chemical Reviews*, Vol. **107**(3) (October, 2007) pp. 718-747
- [22] Zhi L., Müllens K. *Journal of Materials Chemistry*, Vol. **18** (February, 2008) pp. 1472-1484
- [23] S. Schnez, F. Molitor, C. Stampfer, J. Guettinger, I. Shorubalko, T. Ihn, and K. Ensslin, *Appl. Phys. Lett.* **94**, 012107 (2009).
- [24] S. Pavlovi and F. M. Peeters, *Phys. Rev. B* **91**, 155410 (2015).
- [25] M. Chhowalla, H. S. Shin, G. Eda, L. -J. Li, K. P. Loh, H. Zhang, *Nat. Chem.*, **5**, 263-275 (2013).
- [26] Y. Zhang, Y. Zhang, Q. Ji, J. Ju, H. Yuan, J. Shi, T Gao *ACS Nano* **7**, 89638971 (2013)
- [27] K. Nakada, M. Fujita G. Dresselhaus, M. S. Dresselhaus, *Phys. Rev. B* **54**, 17954 (1996).
- [28] Wakabayashi, K., M. Fujita, H. Ajiki, and M. Sigrist, *Phys. Rev. B* **59**, 8271 (1999).
- [29] A. Akhmerov and CWJ Beenakker, *Phys. Rev. B* **77**, 085423 (2008)
- [30] I. Klefogiannis and I. Amanatidis, *Eur. Phys. J. B* **87** (2014) 16.
- [31] Amanatidis E., Klefogiannis I., Katsanos D. E. and Evangelou S. N. *J. Phys.: Condens. Matter* **26** 155601 (2014)
- [32] D. Loss and D. P. Divincenzo, *Phys. Rev. A* **57**, 120 (1998).
- [33] I. Žutić, J. Fabian, and S. Das Sarma, *Rev. Mod. Phys.* **76**, 323 (2004).
- [34] S. A. Wolf, D. D. Awschalom, R. A. Buhrman, J. M. Daughton, S. von Molnár, M. L. Roukes, A. Y. Chtchelkanova, and D. M. Treger, *Science* **294**, 1488 (2001).
- [35] R. Winkler, *Spin-Orbit Coupling Effects in Two-Dimensional Electron and Hole Systems*, Springer Tracts in Modern Physics Vol. 191 (Springer, Berlin, 2003).
- [36] C. L. Kane and E. J. Mele, *Phys. Rev. Lett.* **95**, 226801 (2005).
- [37] König, M. *et al.* *Science* 318, 766770 (2007).
- [38] Tsung-Wei Chen, Zhi-Ren Xiao, Dah-Wei Chiou, and Guang-Yu Guo, *Phys. Rev. B* **84**, 165453 (2011).
- [39] H. Sahin, R. T. Senger, and S. Ciraci, *J. Appl. Phys.* **108**, 074301 (2010).
- [40] Tomoya Ono, Tadashi Ota, and Yoshiyuki Egami, *Phys. Rev. B* **84**, 224424 (2011).
- [41] M. A. Cazalilla, H. Ochoa, and F. Guinea, *Phys. Rev. Lett.* **113**, 077201 (2014).
- [42] Z. Y. Zhu, Y. C. Cheng, and U. Schwingenschlgl, *Phys. Rev. B* **84**, 153402, (2011).

- [43] J. Klinovaja and D. Loss, *Phys. Rev. B* **88**, 075404 (2013).
- [44] Andor Kormanyos, Viktor Zolyomi, Neil D. Drummond, and Guido Burkard, *Phys. Rev. X* **4**, 011034 (2014).
- [45] Yuri D. Lensky, Justin C.W. Song, Polnop Samutpraphoot, and Leonid S. Levitov, *Phys. Rev. Lett.* **114**, 256601 (2015).
- [46] Mingsheng Xu, Tao Liang, Minmin Shi, and Hongzheng Chen, *Chem. Rev.*, 113 **5** 2013.
- [47] Ioannis Kleftogiannis, Chi-Shung Tang, Shun-Jen Cheng, *J. Phys.: Condens. Matter* **27** 205302 (2015).
- [48] M. Inui, S. A. Trugman, and Elihu Abrahams, *Phys. Rev. B* **49**, 3190 (1994).
- [49] S.-Q. Shen, *Topological Insulators: Dirac Equation in Condensed Matters*, Springer Series in Solid-State Sciences **17** (2012).
- [50] C. Lewenkopf and E. Mucciolo, *J. Comput. Electron.* **12**, 203 (2013).